Liquid-mediated crystallization of amorphous GeSn under electron beam irradiation

doi: https://doi.org/10.1063/5.0006416

Liquid-mediated crystallization of amorphous GeSn under electron beam irradiation

Kohei Inenaga[1], Ryo Motomura,[1] Manabu Ishimaru,[1,*] Ryusuke Nakamura,[2] and Hidehiro Yasuda[3]

[1]*Department of Materials Science and Engineering, Kyushu Institute of Technology, Kitakyushu, Fukuoka 804-8550, Japan*

[2]*Department of Materials Science, Osaka Prefecture University, Sakai, Osaka 599-8531, Japan*

[3]*Research Center for Ultra-High Voltage Electron Microscopy, Osaka University, Ibaraki, Osaka 567-0047, Japan*

Abstract

Crystallization processes of amorphous germanium-tin (GeSn) under low-energy electron-beam irradiation were examined using transmission electron microscopy (TEM). Freestanding amorphous GeSn thin films were irradiated with a 100 keV electron beam at room temperature. The amorphous GeSn was athermally crystallized by electron-beam irradiation, when the electron flux exceeded the critical value. Heterogeneous structures consisting of nano- and micro-crystallites were formed after crystallization of amorphous GeSn with ~24 at.%Sn in the as-sputtered amorphous state. *In situ* TEM observations of structural changes under electron-beam irradiation revealed that random nucleation and growth of nanocrystallites occurs at the early stage of crystallization, followed by rapid formation of micro-grains surrounding the nanocrystals. It has been suggested that the growth of micro-grains progresses via supercooled liquid Sn at the amorphous/crystalline interface. The resultant GeSn grains with a size of a few micrometers contained ~15 at.% Sn, much larger than the solubility limit of Sn in Ge (~1 at.%Sn).

*E-mail: ishimaru@post.matsc.kyutech.ac.jp

1. Introduction

Group-IV elements, such as silicon (Si) and germanium (Ge), play an important role in semiconductor industries and are used in semiconductor devices such as solar cells and photodetectors. In particular, polycrystalline Si thin film transistors are a key material in the display industry. Polycrystalline thin films can be produced by crystallization of the amorphous phase. Fabrication of the thin film transistors on plastic substrates is of technological importance for realizing flexible displays, and therefore much effort has been devoted to reducing the crystallization temperature.

As an alternative to Si, Ge has received much attention because of its higher carrier mobility and lower melting temperature than Si. These material properties of Ge enable us to manufacture high-performance thin film transistors at low processing temperatures. Further reduction of the crystallization temperature can be realized by metal doping [1], a phenomenon known as metal-induced crystallization. Of the various metal-induced crystallization techniques for amorphous Ge [1,2], tin (Sn) addition causes the lowest crystallization temperature because of the low eutectic temperature of the Ge-Sn binary system (~231 ºC) [3]. In addition, the synthesis of high Sn concentration GeSn thin films has been extensively studied [4-13], as a way to enhance the carrier mobility and control the electronic band structure of GeSn crystals.

We recently found that supercooled liquid Sn is formed during crystallization of amorphous GeSn under heat treatments [14,15]. We also demonstrated that amorphous Ge thin films are athermally crystallized by inelastic electronic stopping, the so-called electron excitation effects (ionization effects), under low-energy electron-beam irradiation [16-18]. Several researchers have pointed out that the liquid phase at the crystallization front induces abnormal rapid crystallization of amorphous Ge [19-22], motivating us to study the

crystallization processes of amorphous GeSn under electron-beam irradiation.

In the present study, the electron-beam-induced crystallization of amorphous GeSn was directly observed by *in situ* transmission electron microscopy (TEM). It was found that the rapid crystallization occurs at room temperature via liquid Sn at the amorphous/crystalline interface. The resultant GeSn grains are >1 μm in size and contained ~15 at.% Sn, which is much higher than the solubility limit of Sn in Ge (~1.1 at.% at 400 ºC [3]).

2. Experimental

A Ge target of 101 mm in diameter on which 5 mm square Sn chips were placed was used instead of a sintered GeSn target. This was because the Sn concentration can be flexibly varied by changing the number of Sn chips. GeSn thin films with a thickness of 40 nm were deposited on a cleaved rock salt substrate at ambient temperature by radio-frequency magnetron sputtering at a base pressure of $3x10^{-5}$ Pa and an argon partial pressure of 0.7-0.8 Pa. The film and substrate were placed in distilled water, and then the floating film was recovered on a molybdenum TEM grid. Detailed procedures for the sample preparations are described elsewhere [15,23].

The amorphous GeSn thin films were irradiated with 100 keV electrons at room temperature and their crystallization processes were observed *in situ* using a Hitachi H-7000 TEM (Osaka University). Some of the crystallization processes were recorded as movies using a digital camera. The beam current was monitored using a Faraday cage. Because the intensity of the electron beam has a Gaussian-like distribution, the flux described in the present paper represents the intensity at the center of the beam. The flux was gradually increased to determine the threshold value for the amorphous-to-crystalline phase transformation, which was identified by observing the change in diffraction pattern from halo

rings to Debye-Scherrer ones. The Sn concentration of the as-sputtered amorphous GeSn as well as electron-beam-induced crystalline GeSn was measured by energy-dispersive x-ray (EDX) spectroscopy using a JEOL JEM-3000F operated at 300 kV (Kyushu Institute of Technology). Elemental mapping by EDX was performed at an acceleration voltage of 200 kV using JEOL JEM-ARM200CF equipped with dual silicon drift detectors of a 100 mm^2 sensor (Kyushu University).

3. Results and discussion

It was confirmed that amorphous GeSn was immediately crystallized by low-energy electron-beam irradiation, when the electron flux exceeded the critical value, as reported previously [23]. Figure 1 shows structural changes of amorphous GeSn with ~24 at.%Sn under 100 keV electron-beam irradiation for 3 min at room temperature. It is apparent that small crystallites are homogeneously formed in the specimen irradiated at the threshold flux for crystallization, $5.2x10^{21}$ e/m^2s (Fig. 1(a)). The magnified image revealed the formation of fine nanocrystallites with a diameter of <10 nm (Fig. 1(b)). In contrast, heterogeneous microstructures were obtained in the specimen irradiated at higher flux ($2.5x10^{22}$ e/m^2s): small crystallites are observed in the central crystallized region of Fig. 1(c) (Region I), but they are surrounded by large grains where void formation was confirmed (Region II). Similar structures were also observed in single shot laser-induced crystallization in amorphous Ge [22,24,25]. Figure 1(d) shows the magnified image taken from Region I. It was confirmed that a higher flux induces coarse nanocrystallites with a diameter of >100 nm. Hereafter, we call the nanocrystallites generated at the low- and high-flux, respectively, 'fine nano-grains' and 'coarse nano-grains'. The large grains surrounding the coarse nano-grains are several hundred nanometers to a few micrometers in size, as described below, and therefore the grains

in Region II are referred to as 'micro-grains'. The electron-beam-induced crystallization microstructure of sputter-deposited amorphous GeSn is similar to that of amorphous Ge: fine nano-grains appear under low-flux irradiation, whereas coarse nano-grains appear under high-flux irradiation [17,18]. Flux dependent structural changes were also confirmed in amorphous GeSn thin films irradiated with a 75 keV electron beam: the irradiation at a flux of 8.7×10^{21} and 7.9×10^{22} e/m^{2}s induces fine and coarse nano-grains, respectively. In contrast, heterogeneous growth features were not observed. The electron beam was focused to realize a high flux, and it is considered that the beam-illuminated area was narrower than the area where micro-grains are formed.

Figure 2(a) shows a selected-area electron diffraction pattern taken from the region of fine nano-grains. The pattern of Fig. 2(a) reveals Debye-Scherrer rings, which can be indexed from the inside as 111, 220, and 311 of a diamond structure. A closer examination of Fig. 2(a) reveals the presence of a weak halo ring just outside the 111 ring, suggesting the ejection of Sn from the Ge matrix and the formation of amorphous and/or nanocrystalline Sn. A similar Debye-Scherrer ring pattern was also obtained at Region I of Fig. 1(c), but strong Bragg spots due to the coarse nano-grains are overlapped (Fig. 2(b)). It should be noted that extra reflections due to crystalline Sn (β-Sn) are observed just outside the 111 ring. Extra diffraction spots also appear at the position just outside of the 311 ring in Fig. 2(b). The position corresponds to the interplanar spacing of the hypothetical {222} of the diamond cubic structure, and the diffraction peak, which must, in principle, be absent. These spots are attributed to the existence of planar defects, as reported in our previous study [26].

The diffraction patterns taken from Region II of Fig. 1(c) showed a net pattern due to a single crystal. For example, the pattern of Fig. 2(c), obtained from a selected-area with a diameter of ~0.6 μm, corresponds to the (110) reciprocal lattice plane of the diamond

structure. This suggests that a remarkable grain growth occurs in the outer part of the crystallized region. As indicated by rectangles in Fig. 2(c), two additional (110) patterns with a different orientation overlap on the main diffraction pattern. Figure 3 shows a high-resolution TEM image taken from the micro-grain. The electron beam was incident along the [110] direction of the diamond structure. It was confirmed that the grain contains planar defects on the (111) plane, and they were identified as stacking faults and twins, which are often observed in Si and Ge crystallized from amorphous [18,26,27]. The existence of twins causes the overlap of the (110)-type patterns in Fig. 2(c).

Figure 4 shows the magnified bright-field images taken from Region II of Fig. 1(c), along with electron diffraction patterns. The crystallographic orientation of the dark grain marked with "A" satisfies the exact pole axis direction, as shown in the corresponding diffraction pattern. The formation of the grain with a size of >1 μm is confirmed from the diffraction contrast in this image. Electron diffraction patterns taken from the grains (B-D) around the dark region are also shown in Fig. 4. The orientation of the diffraction patterns is different from each other, but the 111-type spots marked with arrows are located at almost the same position. This suggests that a particular orientation relationship exists between the adjacent crystal grains.

To identify the crystallization processes observed here, structural evolution under electron-beam irradiation was recorded using a digital camera with a time resolution of 1/30 sec (see supplemental movie #1). The *in situ* movies are direct recordings of images displayed on the fluorescent screen, and an approximate scale bar is shown in the snapshot of Fig. 5. In the present study, a Faraday cage was inserted just above the fluorescent screen to measure the electron flux during crystallization; and therefore, the flux could not be measured during recording. Because the electron intensity depends on the beam diameter, the flux described for

the movies and their snapshots is the value obtained by a similar beam diameter. Figures 5(a-h) show a series of snapshots of the crystallization processes of amorphous GeSn with ~24 at.%Sn irradiated at a flux of ~2×10^{22} e/m^{2}s. Here, the time at which the crystallization started is defined as "0 sec". Before crystallization, the specimen maintains the amorphous structure (Fig. 5(a)). It was found that the nucleation of crystallites occurs randomly at the center of the irradiated area with maximum flux (Fig. 5(b)), and the grain growth gradually progresses toward the outside (Fig. 5(c)). A large grain suddenly appears adjacent to the coarse nano-grain region (an arrow of Fig. 5(d)), and crystallization proceeds rapidly to surround Region I (Figs. 5(e-g)). Because the crystallization proceeds at the amorphous/crystalline interface, there is an orientation relationship between adjacent crystal grains, as observed in Fig. 4. The crystallization is completed when the crystal regions proceeding clockwise and counterclockwise contact each other (Fig. 5(h)). In Fig. 1(c), contact between the two growth fronts was also observed at the position marked by an arrow. The resultant microstructure is similar to the laser-induced crystallization of amorphous Ge [24], but the growth mode of the micro-grains is different. The electron-beam-induced crystallization of amorphous GeSn progresses circumferentially, whereas the laser-induced crystallization of amorphous Ge proceeds radially toward the outside.

Amorphous GeSn thin films with ~24 at.%Sn were crystallized at ~230 ºC during heat treatments [15]. The heating effects under a uniformly distributed electron beam with a radius of r_0 can be estimated by the following equation [28]: $\Delta T = V_0 I_0 / \pi k r_0$, where ΔT is the temperature rise, V_0 the acceleration voltage, I_0 the beam current, and k the thermal conductivity (5.1×10^{-1} Wm^{-1}K^{-1} for amorphous Ge (no available data for amorphous GeSn) [29]). Under the irradiation conditions of Fig. 1(c) (V_0 = 100 kV and I_0 = 0.2 nA), the temperature rise was calculated to be ~1 K. Furthermore, the rapid crystallization occurs in

the outer part of the crystallized region where the electron flux is smaller than the central region. These results suggest that the formation of the micro-grains in Region II is not due to rise in temperature. To identify the crystallization mechanism, we examined the distributions of Sn in the crystallized region. Figures 6(a,a',a'') show a high-angle annular dark-field (HAADF) image and elemental maps taken from the interface between Regions I and II. The elemental maps were obtained using the characteristic x-rays of (a') Ge-*K* and (a'') Sn-*L*. In the present study, 40-nm-thick freestanding amorphous GeSn thin films were supported on the molybdenum TEM grid, and therefore the thickness presumably varied depending on the location because of the sample bending after crystallization. This means that the brightness of the HAADF image reflects not only the atomic concentration but also the specimen thickness. The elemental map of Fig. 6(a'') reveals that small Sn precipitates are densely dispersed in the coarse nano-grain region, whereas large Sn precipitates are sparsely present in the micro-grain region. A remarkable Sn aggregation occurs between Regions I and II. Figures 6(b,b',b'') show a HAADF image and elemental maps taken from the amorphous/crystalline interface after crystallization. An Sn-rich layer was formed between the micro-grain and amorphous regions.

Our previous studies suggested that the crystallization of amorphous Ge and GeSn under low-energy electron-beam irradiation is induced by electron excitation effects (ionization effects) [16,17,23]. The ejection of Sn from the Ge matrix occurs during the crystallization because Ge and Sn show a eutectic phase-equilibrium in which the solid solution of Ge can include at most 1.1 at.%Sn [3]. A halo ring caused by an amorphous phase was observed in the diffraction pattern of Fig. 2(a), suggesting that the once formed liquid phase has solidified. This means that the ejected Sn exists as a liquid phase under electron irradiation. The incident electrons inelastically interact with the target atom, and ionization

occurs because of the ejection of the inner-shell electrons. The ionization cross section of Sn is larger than that of Ge, and it is thought that a liquid state, with higher energy than the crystalline state, is induced. In fact, the non-equilibrium state is often realized by electron excitation effects [30,31].

The accumulation of Sn atoms gradually occurs during the crystallization. It should be noted that the crystallization front of Figs. 5(e-g) shows the homogeneous dark contrast during crystallization, suggesting the formation of a liquid phase. In the case of amorphous and liquid phases, the contrast of the bright-field image depends mainly on the atomic number and density. A remarkable dark contrast at the growth front suggests that Sn concentration is much larger than that of the GeSn matrix. A halo ring observed in the electron diffraction pattern of Fig. 2(a) is close to the location of Bragg reflections of β-Sn. It is similar to the patterns obtained from the GeSn thin film, including a supercooled liquid Sn [15], supporting the formation of high Sn concentration liquid. EDX analyses revealed that a significant Sn segregation occurs at the dark regions after crystallization. Although it is difficult to analyze the composition of the growth front during crystallization, the region is considered to be mostly Sn, based on the EDX analysis after crystallization. Indeed, the absence of a lamellar structure also supports this possibility. The formation of homogeneous GeSn crystals without a lamellar structure has been confirmed in the liquid Sn-driven crystallization of amorphous GeSn [32]. These results suggest that a supercooled liquid Sn is formed at the crystallization front, and the crystallization progresses via this liquid phase. There are some regions where no dark contrast is observed at the moving front in the supplemental movie. This is either because the liquid layer is too thin to be observed or because the amorphous GeSn is directly crystallized. However, our claim that the presence of a liquid phase at the growth front promotes crystallization remains unchanged.

It has been reported that instantaneous processes, such as laser irradiation [24,25,33,34], flash-lamp annealing [35,36], electron-beam heating [37], and mechanical stimulation [38,39], induce abnormal rapid crystallization, the so-called explosive crystallization. Although the mechanism of explosive crystallization is still controversial, several researchers have proposed that the crystallization in Si [40,41] and Ge [19-22] proceeds via a metastable liquid phase at the amorphous/crystalline interface. The growth rate in the present study (a few μm/s) was much smaller than that of the explosive crystallization (several m/s), but it was suggested that the supercooled liquid Sn at the crystallization front plays a pivotal role in progressing the rapid crystallization.

To confirm the existence of Sn precipitates in nanoscale, the elemental mapping of a micro-grain was performed with a higher magnification than Figs. 6(a',a'',b',b''). Figures 6(c') and 6(c'') show the Ge and Sn distributions, respectively, taken from the region where no remarkable Sn precipitates were detected by the elemental mapping of Figs. 6(a'',b''). Note that the fluctuation of Ge and Sn concentrations is due to the thickness difference, as described. It is apparent that the Sn precipitates are highly suppressed, and Sn precipitate-free regions with a size of >2 μm are formed. Figure 6(d) shows an EDX spectrum taken from the point indicated in Fig. 6(c) where no Sn precipitates exist. In addition to the characteristic x-rays associated with Ge, remarkable Sn signals are detected. Based on the electron diffraction experiments and elemental mapping, it can be concluded that Sn atoms are substitutionally incorporated into Ge with a diamond structure. From a quantitative analysis of the EDX spectra, the Sn concentration was estimated to be ~19 at.%Sn. We also took EDX spectra from several other grains and confirmed that the Sn concentration is from ~15 to ~20 at.%Sn. From the lattice parameter (a = 0.578 nm), the Sn concentration (x) was also estimated to be ~15 at.%Sn based on the Vegard law ($a_{GeSn}=xa_{\alpha\text{-Sn}}+(1-x)a_{Ge}$, where $a_{\alpha\text{-Sn}}$ =

0.6493 nm and a_{Ge} = 0.5658 nm). These values are much higher than the solubility limit of Sn in crystalline Ge (~1 at.%Sn at 400 ºC), according to the equilibrium phase diagram of the Ge-Sn binary system [3].

It is considered that the rapid formation of the micro-grains is induced when Sn concentration exceeds a certain threshold value. To confirm the validity of this speculation, we examined the crystallization processes of amorphous GeSn with ~14 and ~31 at.%Sn under 100 keV electron-beam irradiation at room temperature. Figure 7 shows a series of bright-field TEM images during crystallization, taken from the movie (see supplemental movies #2 and #3). In the low-Sn concentration specimen irradiated at a flux of ~5x10^{22} e/m^2s, a random nucleation of crystallites initially occurs and the grain growth gradually progresses toward the outside (Fig. 7(a)). The resultant structures are similar to those formed at the early stage of crystallization of amorphous GeSn with ~24 at.%Sn. In contrast, rapid growth proceeds as soon as the nuclei are formed in the high-Sn concentration specimen irradiated at a flux of ~1x10^{22} e/m^2s (Fig. 7(b)), and the irradiated area is covered with micro-grains. Again, it was confirmed that liquid Sn is formed at the crystallization front of Fig. 7(b).

Chikita *et al.* [32] examined lateral solid phase crystallization of GeSn and reported that the growth velocity rapidly increases with the Sn concentration: 0.13 μm/h for 14 at.%Sn, 27 μm/h for 20 at.%Sn, and 1100 μm/h for 23 at.%Sn at 220 ºC. The growth velocity of the latter is much larger than the others. Sn segregation in the amorphous matrix during thermal annealing was detected in the specimens with >25 at.% Sn by *in situ* TEM observations using a heating holder [15]. In addition, the formation of liquid Sn under electron beam irradiation was observed in the GeSn thin films with Sn concentration of >23 at.% [23]. Our present study demonstrated that the Sn concentration is an important factor to induce the liquid-mediated rapid crystallization of amorphous GeSn, and it is thought that the threshold

concentration for rapid crystallization is ~25 at.%Sn.

4. Conclusions

We prepared amorphous GeSn thin films by radio-frequency magnetron sputtering and examined their crystallization behavior under electron-beam irradiation by *in situ* TEM. A 100 keV electron beam induces crystallization of amorphous GeSn at room temperature. The crystallization processes were highly dependent on the initial Sn concentration of the amorphous phase. Random nucleation and growth of nanocrystallites occurred in amorphous GeSn with ~14 at.%Sn, while rapid growth of micro-grains immediately started after the nucleation in the amorphous matrix with ~31 at.%Sn. Heterogeneous structures consisting of the nanocrystallites and micro-grains were formed after crystallization of amorphous GeSn with ~24 at.%Sn. The ejection of Sn atoms occurred during crystallization, and supercooled liquid Sn was formed at the crystallization front: liquid-mediated crystallization plays an important role in the formation of the micro-grains. Our present study demonstrated that >1 μm GeSn crystals with ~15 at.%Sn can be synthesized at room temperature by electron-beam irradiation.

Supplementary material

See supplementary material for the crystallization processes of amorphous GeSn under electron-beam irradiation.

Acknowledgments

We acknowledge financial support by Japan Society for the Promotion of Science (JSPS) KAKENHI (Grant No. 19H02463). A part of this work was supported by "Advanced

Characterization Nanotechnology Platform, Nanotechnology Platform Program of the Ministry of Education, Culture, Sports, Science and Technology (MEXT), Japan" at the Research Center for Ultra-High Voltage Electron Microscopy in Osaka University and at the Ultramicroscopy Research Center in Kyushu University. We are grateful to Takaaki Toriyama of Kyushu University for his helpful support in transmission electron microscopy analysis and Masayuki Okugawa of Osaka University for his contribution of preparing amorphous GeSn specimens.

Availability of data

The data that support the findings of this study are available within the article and its supplementary material.

References

[1] W. Knaepen, S. Gaudet, C. Detavernier, R. L. Van Meirhaeghe, J. J. Sweet, and C. Lavoie, J. Appl. Phys. **105**, 083532 (2009).

[2] S. Zaima, O. Nakatsuka, N. Taoka, M. Kurosawa, W. Takeuchi, and M. Sakashita, Sci. Technol. Adv. Mater. **16**, 043502 (2015).

[3] M. Hansen and K. Anderko, *Constitution of Binary Alloys* (McGraw-Hill, New York, 1958).

[4] M. Kurosawa, N. Taoka, M. Sakashita, O. Nakatsuka, M. Miyao, and S. Zaima, Appl. Phys. Lett. **103**, 101904 (2013).

[5] M. Kurosawa, N. Taoka, H. Ikenoue, O. Nakatsuka, and S. Zaima, Appl. Phys. Lett. **104**, 061901 (2014).

[6] W. Takeuchi, N. Taoka, M. Kurosawa, M. Sakashita, O. Nakatsuka, and S. Zaima, Appl. Phys. Lett. **107**, 022103 (2015).

[7] R. R. Lieten, J. W. Seo, S. Decoster, A. Vantomme, S. Peters, K. C. Bustillo, E. E. Haller, M. Menghini, and J.-P. Locquet, Appl. Phys. Lett. **102**, 052106 (2013).

[8] H. Chikita, R. Matsumura, Y. Kai, T. Sadoh, and M. Miyao, Appl. Phys. Lett. **105**, 202112 (2014).

[9] R. Matsumura, H. Chikita, Y. Kai, T. Sadoh, H. Ikenoue, and M. Miyao, Appl. Phys. Lett. **107**, 262106 (2015).

[10] K. Toko, N. Oya, N. Saitoh, N. Yoshizawa, and T. Suemasu, Appl. Phys. Lett. **106**, 082109 (2015).

[11] M. Kim, W. Fan, J.-H. Seo, N. Cho, S.-C. Liu, D. Geng, Y. Liu, S. Gong, X. Wang, W. Zhou, and Z Ma, Appl. Phys. Express **8**, 061301 (2015).

[12] N. Uchida, T. Maeda, R. R. Lieten, S. Okajima, Y. Ohishi, R. Takase, M. Ishimaru, and

J.-P. Locquet, Appl. Phys. Lett. **107**, 232105 (2015).

[13] N. Uchida, J. Hattori, R. R. Lieten, Y. Ohishi, R. Takase, M. Ishimaru, K. Fukuda, T. Maeda, and J.-P. Locquet, J. Appl. Phys. **126**, 145105 (2019).

[14] R. Takase, M. Ishimaru, N. Uchida, T. Maeda, K. Sato, R. R. Lieten, and J.-P. Locquet, J. Appl. Phys. **120**, 245304 (2016).

[15] M. Higashiyama, M. Ishimaru, M. Okugawa, and R. Nakamura, J. Appl. Phys. **125**, 175703 (2019).

[16] M. Okugawa, R. Nakamura, M. Ishimaru, K. Watanabe, H. Yasuda, and H. Numakura, J. Appl. Phys. **119**, 214309 (2016).

[17] M. Okugawa, R. Nakamura, M. Ishimaru, H. Yasuda, and H. Numakura, J. Appl. Phys. **120**, 134308 (2016).

[18] M. Okugawa, R. Nakamura, H. Numakura, A. Heya, N. Matsuo, and H. Yasuda, Jpn. J. Appl. Phys. **58**, 045501 (2019).

[19] H. J. Leamy, W. L. Brown, G. K. Celler, G. Foti, G. H. Gilmer, and J. C. C. Fan, Appl. Phys. Lett. **38**, 137 (1981).

[20] C. Grigoropoulos, M. Rogers, S. H. Ko, A. A. Golovin, and B. J. Matkowsky, Phys. Rev. B **73**, 184125 (2006).

[21] G. C. Egan, T. T. Rahn, A. J. Rise, H.-Y. Cheng, S. Raoux, G. H. Campbell, and K. Santala, J. Appl. Phys. **126**, 105110 (2019).

[22] G. C. Egan, T. W. Heo, A. Samanta, and G. H. Campbell, Acta Mater. **179**, 190 (2019).

[23] T. Kimura, M. Ishimaru, M. Okugawa, R. Nakamura, and H. Yasuda, Jpn. J. Appl. Phys. **56**, 100307 (2017).

[24] L. Nikolova, M. J. Stern, J. M. MacLeod, B. W. Reed, H. Ibrahim, G. H. Campbell, F. Rosei, T. LaGrange, and B. J. Siwick, J. Appl. Phys. **116**, 093512 (2014).

[25] M. K. Santala, S. Raoux, and G. H. Campbell, Appl. Phys. Lett. **107**, 252106 (2015).

[26] M. Okugawa, R. Nakamura, A. Hirata, M. Ishimaru, H. Yasuda, and H. Numakura, J. Appl. Crystallogr. **51**, 1467 (2018).

[27] J. R. Parsons and C. W. Hoelke, Philos. Mag. A **50**, 329 (1985).

[28] M. Liu, L. Xu, and X. Lin, Scanning **16**, 1 (1994).

[29] D. G. Cahill and R. O. Pohl, Phys. Rev. B **37**, 8773 (1988).

[30] H. Yasuda, H. Mori, and J. G. Lee, Phys. Rev. B **70**, 214105 (2004).

[31] H. Yasuda, A. Tanaka, K. Matsumoto, N. Nitta, and H. Mori, Phys. Rev. Lett. **100**, 105506 (2008).

[32] H. Chikita, R. Matsumura, Y. Kai, T. Sadoh, and M. Miyao, Appl. Phys. Lett. **105**, 202112 (2014).

[33] U. Köster, Phys. Status Solidi A **48**, 313 (1978).

[34] H.-D. Geiler, E. Glaser, G. Götz, and M. Wagner, J. Appl. Phys. **59**, 3091 (1986).

[35] K. Ohdaira, T. Fujiwara, Y. Endo, S. Nishizaki, and H. Matsumura, J. Appl. Phys. **106**, 044907 (2009).

[36] K. Ohdaira and H. Matsumura, Thin Solid Films **524**, 161 (2012).

[37] J. R. Parsons and C. W. Hoelke, Philos. Mag. A **50**, 329 (1985).

[38] T. Takamori, R. Messier, and R. Roy, Appl. Phys. Lett. **20**, 201 (1972).

[39] T. Takamori, R. Messier, and R. Roy, J. Mater. Sci. **8**, 1809 (1973).

[40] M. O. Thompson, G. J. Galvin, J. W. Mayer, P. S. Peercy, J. M. Poate, D. C. Jacobson, A. G. Cullis, and N. G. Chew, Phys. Rev. Lett. **52**, 2360 (1984).

[41] P. A. Stolk, A. Polman, and W. C. Sinke, Phys. Rev. B **47**, 5 (1993).

Figure captions

Figure 1. Bright-field TEM images of the specimens crystallized by electron-beam irradiation. Amorphous GeSn thin films with ~24 at.%Sn were irradiated with a 100 keV electron beam at a flux of (a,b) 5.2×10^{21} e/m^{2}s (critical flux for amorphization) and (c,d) 2.5×10^{22} e/m^{2}s. Homogeneous nanocrystallites (fine nano-grain) are formed in (a), while the small crystallites (coarse nano-grain) in the central crystallized region are surrounded by large crystal grains (micro-grains) in (c). The arrow in (c) indicates the position where two growth fronts contact. (b,d) Magnified images taken from the central crystallized region of (a,c).

Figure 2. Selected-area electron diffraction patterns taken from the crystallized region: (a) fine nano-grains, (b) coarse nano-grains (Region I), and (c) micro-grains (Region II). The selected-area of (a) and (b) is ~1.2 μm in diameter. Debye-Scherrer rings due to a diamond structure appear in diffraction patterns taken from the center of the crystallized region. Note that a weak halo ring and extra Bragg spots due to Sn segregation exist in (a) and (b), respectively. The diffraction pattern of (c) was obtained from a micro-grain with a selected-area of ~0.6 μm. The rectangles denote the (110) patterns with a different orientation.

Figure 3. A high-resolution TEM image of the coarse grain, viewed along the [110] direction. Planar defects, such as stacking faults and twins, exist on the (111) plane.

Figure 4. A magnified bright-field TEM image taken from the coarse grains existing at the outside of the crystallized region. The diffraction contrast reveals the formation of GeSn crystals with a size of >1 μm. Electron diffraction patterns were taken from the locations indicated by "A"-"D". The electron beam is incident along the [110] direction for grain A.

The 111-type spots marked with arrows are observed in all the diffraction patterns, suggesting the existence of a particular orientation relationship between the adjacent grains.

Figure 5. (Color online) Structural evolution of amorphous GeSn under electron-beam irradiation. (a) Before crystallization (<0 sec), (b) 4.23 sec, (c) 20.90 sec, (d) 24.80 sec, (e) 27.97 sec, (f) 29.43 sec, (g) 33.33 sec, and (h) 38.33 sec after crystallization. "0 sec" is the time when crystallization started. Nanocrystallites are first formed under electron-beam irradiation, and then a significant grain growth proceeds rapidly around the central coarse nano-grain region. (Also see the supplemental movie #1.)

Figure 6: (Color online) (a,b,c) HAADF-STEM images and elemental maps of (a'b'c') Ge and (a'',b'',c'') Sn. (a,a',a'') Center and (b,b',b'') edge of the crystallized area. (c,c',c'') HAADF-STEM image and EDX elemental maps taken from the micro-grain. (d) EDX spectrum taken from the location indicated by a circle in (c). In addition to the characteristic x-rays of Ge, remarkable Sn signals are observed.

Figure 7. Electron-beam-induced crystallization processes of amorphous GeSn with (a) ~14 and (b) ~31 at.%Sn in the as-sputtered state. On one hand, random nucleation occurs at the electron-beam irradiated area and the crystallized region gradually extends in (a). On the other hand, rapid grain growth immediately progresses after the nucleation, and the irradiated area is covered with micro-grains in (b). (Also see the supplemental movies #2 and #3.)

AIP Publishing

Journal of Applied Physics

ACCEPTED MANUSCRIPT

PLEASE CITE THIS ARTICLE AS DOI: 10.1063/5.0006416

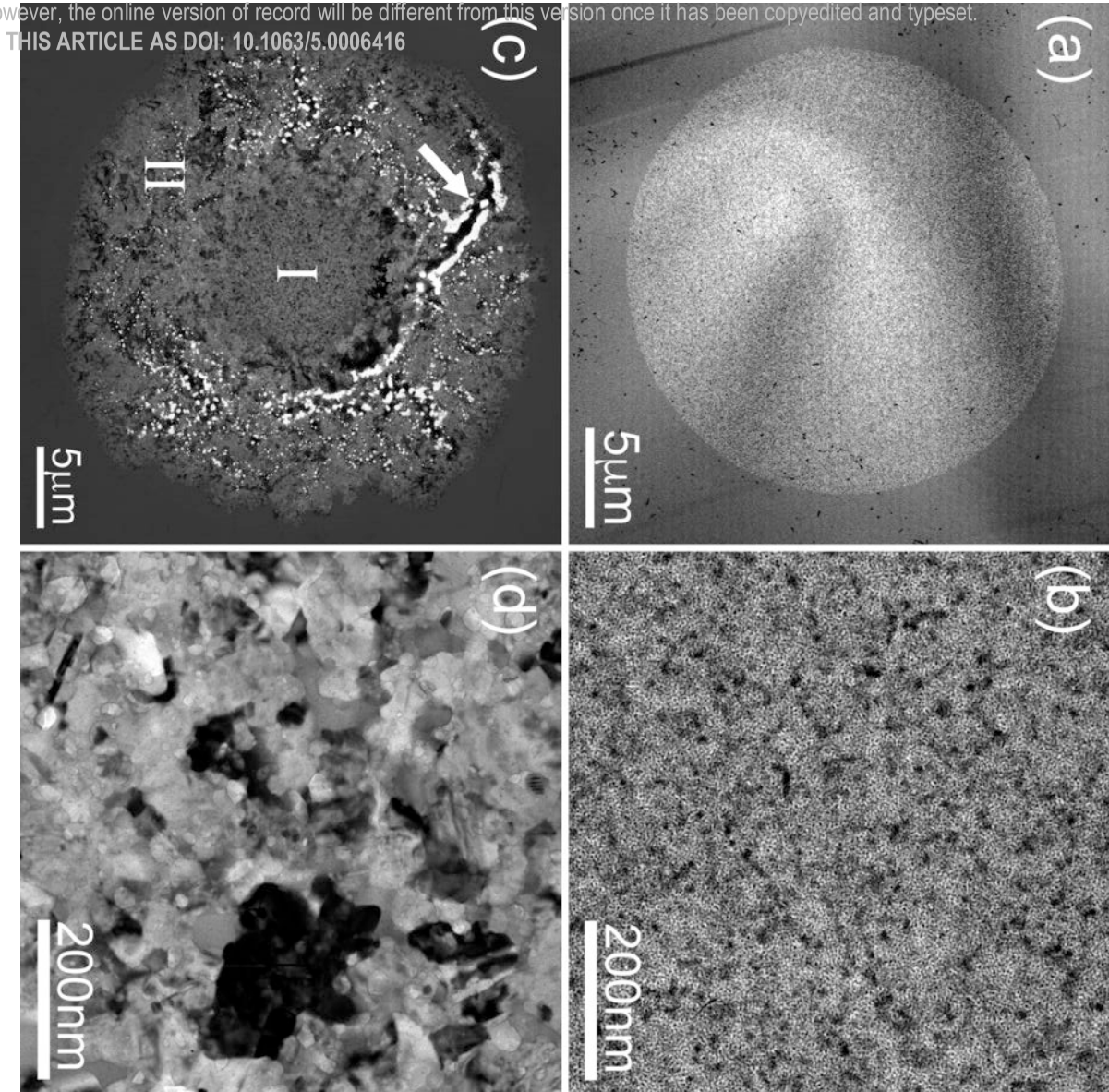

AIP Publishing

Journal of Applied Physics

ACCEPTED MANUSCRIPT

PLEASE CITE THIS ARTICLE AS DOI: 10.1063/5.0006416

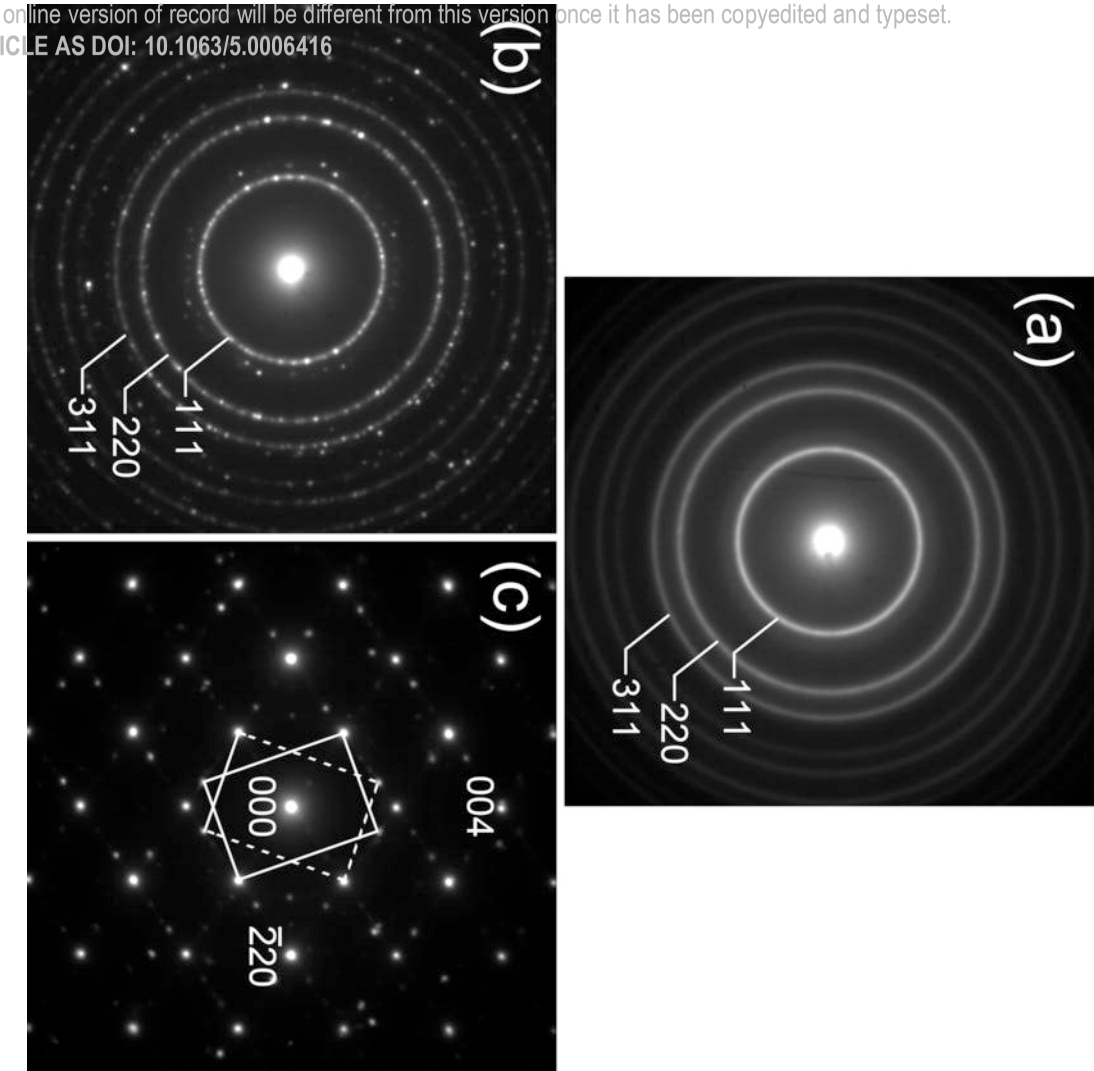

AIP Publishing

Journal of Applied Physics

ACCEPTED MANUSCRIPT

This is the author's peer reviewed, accepted manuscript. However, the online version of record will be different from this version once it has been copyedited and typeset.
PLEASE CITE THIS ARTICLE AS DOI: 10.1063/5.0006416

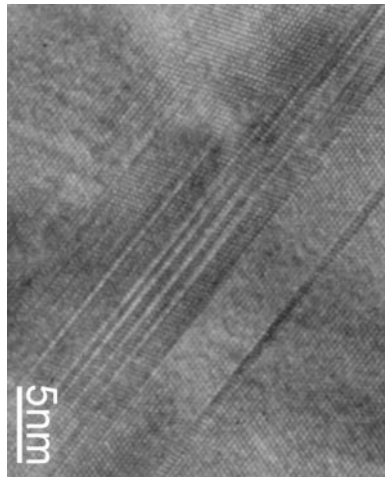

AIP Publishing

Journal of Applied Physics

ACCEPTED MANUSCRIPT

ARTICLE THIS ARTICLE AS DOI: 10.1063/5.0006416

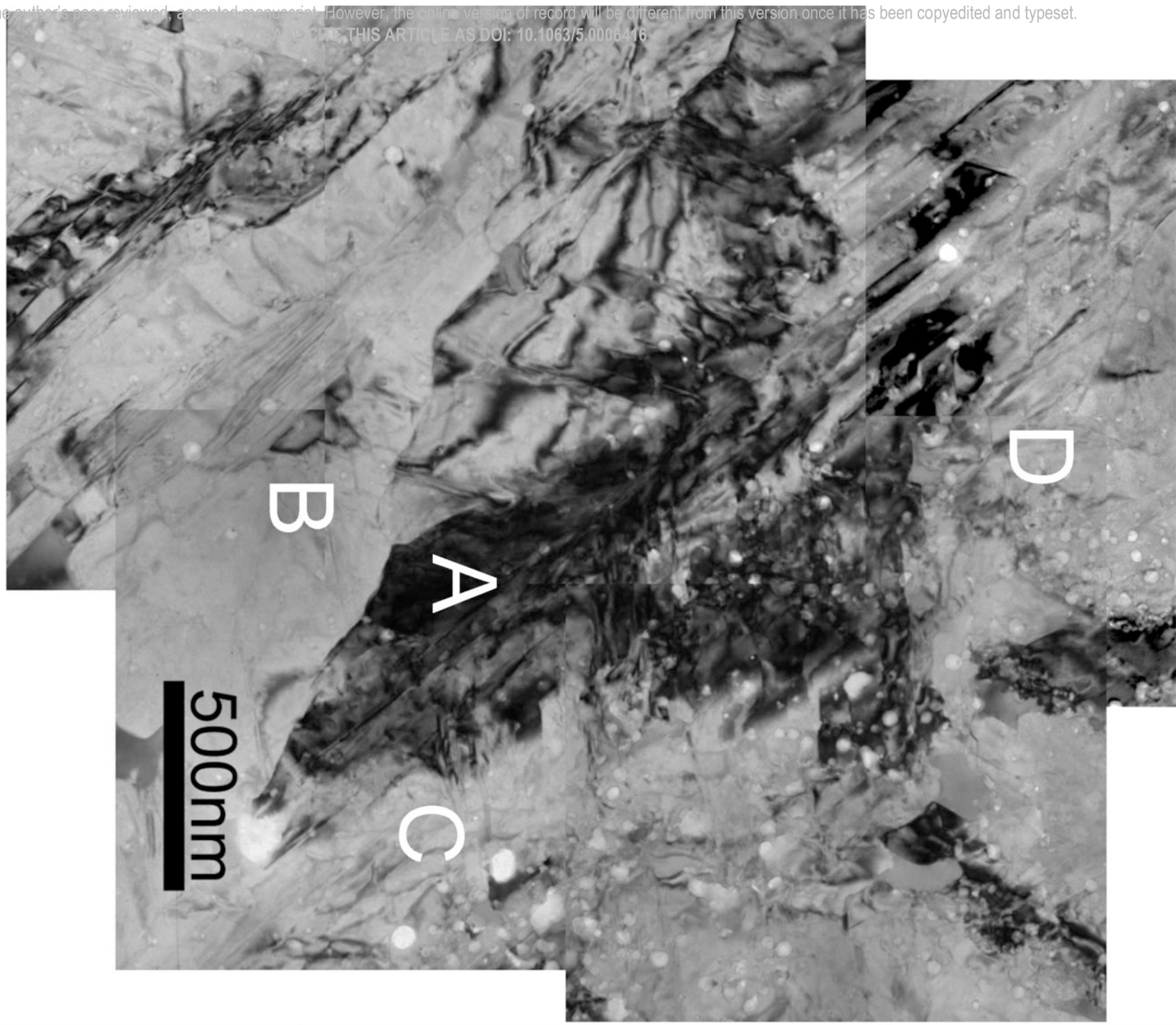

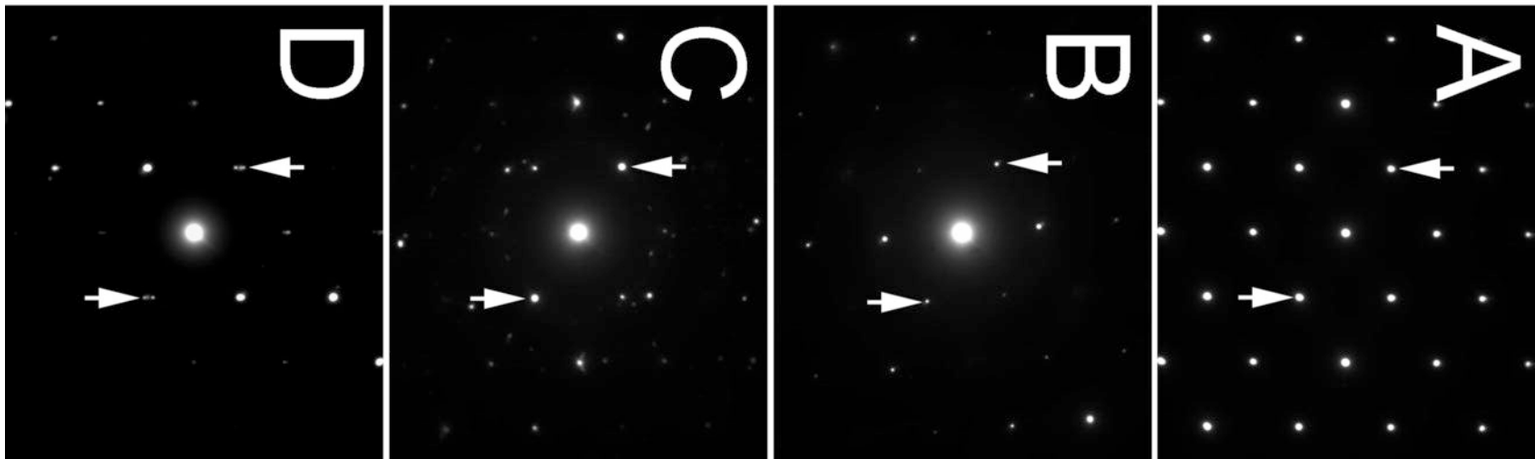

AIP Publishing

Journal of Applied Physics

ACCEPTED MANUSCRIPT

PLEASE CITE THIS ARTICLE AS DOI: 10.1063/5.0006416

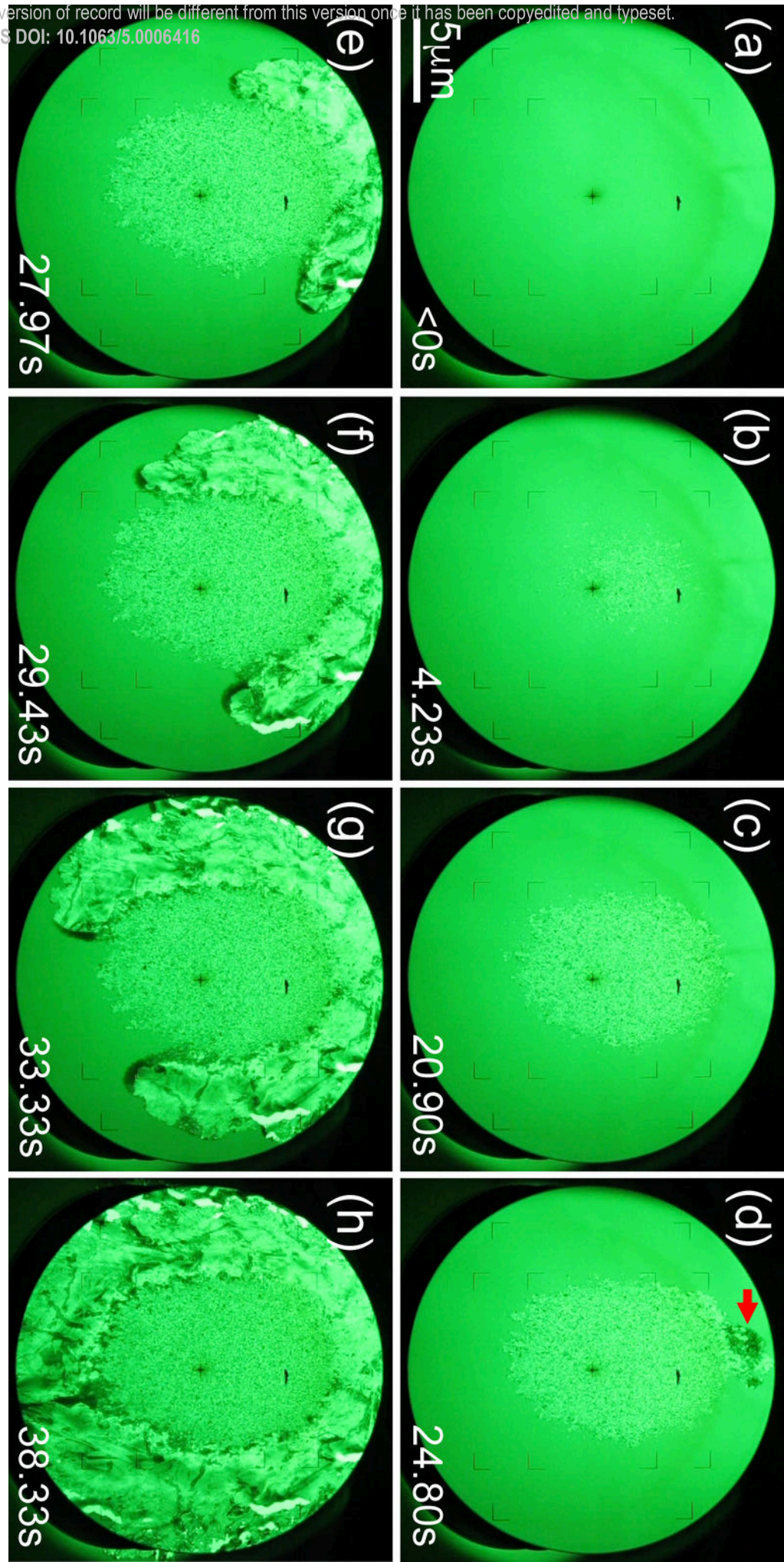

Journal of Applied Physics

AIP Publishing

Journal of Applied Physics

ACCEPTED MANUSCRIPT

This is the author's peer reviewed, accepted manuscript. However, the online version of record will be different from this version once it has been copyedited and typeset.
PLEASE CITE THIS ARTICLE AS DOI: 10.1063/5.0006416